The Composite Spectrum of the Little Red Dots from an Inner Standard Disk and an Outer Gravitationally Unstable Disk

Chenxuan Zhang[1], Qingwen Wu[1*], Xiao Fan[2], Luis C. Ho[3,4], Jiancheng Wu[1], Huanian Zhang[1], Bing Lyu[3], Xinwu Cao[5], Jianmin Wang[6,7,8]

[1]Department of Astronomy, School of Physics, Huazhong University of Science and Technology, Luoyu Road, Wuhan, 430074, Hubei, China.
[2]School of Physics and Technology, Wuhan University, Luoyu Road, Wuhan, 430072, Hubei, China.
[3]Kavli Institute for Astronomy and Astrophysics, Peking University, Yiheyuan Road, Beijing, 100871, Beijing, China.
[4]Department of Astronomy, School of Physics, Peking University, Yiheyuan Road, Beijing, 100871, Beijing, China.
[5]Institute for Astronomy, School of Physics, Zhejiang University, Yuhangtang Road, Hangzhou, 310027, China, China.
[6]Key Laboratory for Particle Astrophysics, Institute of High Energy Physics, Chinese Academy of Sciences, Yuquan Road, Beijing, 100049, Beijing, China.
[7]National Astronomical Observatories of China, Chinese Academy of Sciences, Datun Road, Beijing, 100101, Beijing, China.
[8]School of Astronomy and Space Science, University of Chinese Academy of Sciences, Yuquan Road, Beijing, 100049, Beijing, China.

*Corresponding author(s). E-mail(s): qwwu@hust.edu.cn;

Abstract

One of the most mysterious results from observations of the James Webb Space Telescope (JWST) is the detection of numerous, high-redshift, very red, extremely compact, broad-line sources termed "little red dots" (LRDs). It is unclear whether the LRDs belong to

an active galactic nucleus (AGN) or simply a collection of very compact star clusters. We build spectral energy distributions (SEDs) for 29 LRDs at $z \approx 3-8.5$ based on JWST photometric and spectroscopic observations. We find that the V-shaped SEDs of these LRDs exhibit a roughly similar break frequency at $\nu_{\rm b} = 10^{14.96\pm0.06}$ Hz, which corresponds to $\lambda_{\rm b} = 3287^{+487}_{-424}$Å in the rest frame. We propose that this unique SED can be explained by the combination of an inner standard disk and an outer gravitationally unstable accretion disk with Toomre parameter $Q \sim 1$. The outer disk has a temperature of $\sim 2000-4000$ K for typical AGN parameters, which can well reproduce the near-infrared to optical bump as observed in LRDs. This model can naturally explain the strong infrared to optical emission and the V-shaped SED with a similar break frequency $\simeq 10^{15}$ Hz for LRDs without invoking strong dust extinction or unusual stellar contribution from a host galaxy. Most LRDs stay in sub-Eddington state based on the SED modeling, which are intrinsically weak in X-rays.

Keywords: Active galactic nucleus (16), High-redshift galaxy(734), JWST(2291), Supermassive black hole (1663)

1 Introduction

James Webb Space Telescope (JWST) is opening up a new era in the study of the early Universe, thanks to its remarkable sensitivity and angular resolution at infrared wavelength [1]. One of the most surprising results from JWST is the discovery of numerous faint, optically red and extremely compact sources ($R_{\rm e} \approx 100$ pc) [2–4]. These sources are referred to as "Little Red Dots" [3, 5–7], which are widely considered as candidates for high-redshift active galactic nuclei (AGNs) based on their broad emission lines, and can play an important role in understanding the evolution of galaxies and supermassive black holes at cosmic dawn [6–11]. The LRDs exhibit spectral energy distributions (SEDs) characterized by a "V-shaped" continuum with a luminous red component and a faint blue component in the rest-frame spectrum, which is notably different from that of local AGNs [3, 5, 7]. Furthermore, the LRDs are less variable and are X-ray weaker compared to classical AGNs [12–14]. Interpreting the LRD SEDs remains difficult, which prevents us from further understanding the possible SMBH growth or galaxy evolution in high redshift [15, 16]. The common AGN-only or galaxy-only models cannot adequately describe the two distinct spectral components in V-shaped SEDs. For the AGN-only scenario, the red/optical component is dust-reddened AGNs due to the dust in the torus and/or interstellar medium, [e.g., 8, 17]. It has also been proposed that the LRDs may be powered by the pure dusty starburst galaxies [18–21]. Alternatively, some studies also consider the co-existence of AGNs and galaxies: either a galaxy dominates the rest-frame UV SED while a reddened AGN contributes in the rest-frame infrared to optical range; or the AGN contributes significantly to the rest-frame UV while a dusty stellar population contributes in the rest-frame UV SED [17, 18, 21]. A fraction of LRDs exhibit a clear Balmer break in their spectra, which

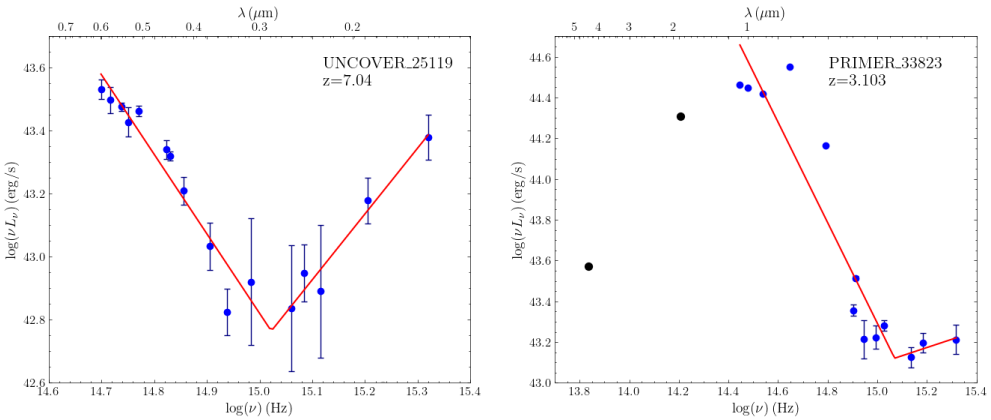

Fig. 1: Example of broken-power-law fits for two LRDs of UNCOVER 25119 and PRIMER 33823 (see Methods 2.2 for other 27 LRDs). The two mid-infrared MIRI data (black points) of PRIMER 33823 are not included in the fitting since they deviate from the typical broken-power-law model in the optical to UV waveband, as clearly found in most LRDs.

indicates either an old stellar population [22, 23] or extremely dense gas surrounding an AGN [24–26]. Most of these models predict significant dust emission in LRDs to explain their distinctive V-shaped SEDs. However, observations reveal no detectable mid- to far-infrared emission, suggesting a lack of both hot and cold dust components [27–29], which contradicts the attenuated luminosities as anticipated in these models.

In this paper, we build the SEDs based on the photometric and spectroscopic data for a sample of 29 LRDs, all exhibiting broad emission lines. We firstly fit the V-shaped SED in the rest frame with a simple broken-power-law model (see Methods 2.2 for the fittings). We present the fittings for two LRDs, UNCOVER 25119 and PRIMER 33823, as examples in Figure 1, which illustrate the characteristic V-shaped SEDs and bumped infrared-to-optical SEDs, respectively. In the linear fitting, we exclude photometric data points with frequencies higher than the Lyman limit, Signal-to-Noise Ratio (SNR) less than 1, or data significantly affected by emission lines. Additionally, the long-wavelength MIRI data of PRIMER 33823 are disregarded in the linear fitting due to their evident deviation from the V-shaped spectrum, which will be addressed in a more physically motivated model. Interestingly, we find that the break frequencies in the V-shaped SEDs fall within a narrow range, from $\sim 10^{14.8}$ to $10^{\sim 15.1}$ Hz (or the inflection wavenlength from 2600-3800 Å). We present the distribution of the inflection wavelength in the left panel of Figure 2, where $\lambda_{\rm b} = 3287^{+487}_{-424}$ Å or $\nu_{\rm b} = 10^{14.96\pm0.06}$ Hz. These fitting results suggest LRDs exhibit a similar break frequency in the rest-frame V-shaped SED. We present the SEDs for 29 LRDs in the right panel of Figure 2, which are normalized at the inflection wavelength $\lambda_{\rm b}$.

We explore the physical mechanism underlying this special feature of SEDs. The standard accretion disk is believed to power luminous AGNs [30]. It is well known that the outer part of the standard disk, beyond a critical radius is prone to suffer

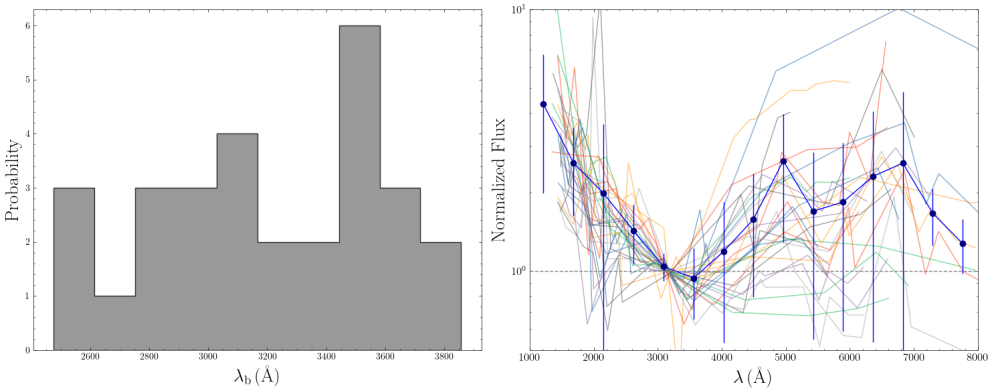

Fig. 2: Left panel shows the histogram for the inflection wavelength in V-shaped LRD SEDs. The right panel shows the normalized SEDs at $\lambda_b = 3287$Å, corresponding to the break frequency of $\nu_b = 10^{14.96}$ Hz, where the binned value with a standard error is also shown as black dots.

gravitational instability if Toomre parameter $Q = c_s\Omega/\pi G\Sigma < 1$, where c_s, Ω, G and Σ are sound speed, angular velocity, gravitational constant and disk surface density respectively [31]. In AGNs, the gravitational instability of the accretion disk provides a mechanism for forming nuclear stars and enriching the metals in the central part of galaxies as indicated by the broad emission lines [e.g., 32–35]. The feedback from the stellar process (e.g., supernova, stellar wind) and turbulent heating can balance radiative cooling of the accretion disk, allowing the outer unstable disk to eventually self-regulate at $Q \sim 1$ [e.g., 36–38], where the additional heating will increase the disk temperature in the outer disk and mainly radiate in the near infrared to optical wavebands [36]. The structure of the accretion disk and the radiation spectrum can be derived from the SMBH mass, $M_{\rm BH}$, accretion rate, $\dot{M}$, viscosity parameter, α, and outer radius of the accretion disk, $R_{\rm out}$. In this work, the viscosity parameter $\alpha = 0.1$ is adopted. In Figure 3, we present a cartoon picture (top panel), disk temperature (middle panel), and emitted spectrum (bottom panel) of this disk for typical AGN parameters. The disk temperature of the outer marginally unstable disk is around 2000-4000 K in the range of $10^{4-6}R_{\rm g}$ ($R_{\rm g} = GM_{\rm BH}/c^2$ is gravitational radius, and c is light speed), which is much hotter than the typical temperature of dust torus. The blackbody emission of the outer disk with this temperature mainly radiates in the near infrared to optical waveband, which can explain the red excess in the spectra of the LRDs. This model predicts a V-shaped SED, in which the near-infrared to optical and optical to UV emission originates from the outer marginally unstable disk and the inner standard accretion disk, respectively.

We further fit the unique LRD SEDs using the model described above for all sources in our sample using the Markov chain Monte Carlo (MCMC) method implemented in emcee [39]. We adopt the SMBH mass estimated from broad emission lines, treating only two parameters, $\dot{M}$ and $R_{\rm out}$, as free variables that can be constrained through SED modeling. In Figure 4, we present an example of the modeling

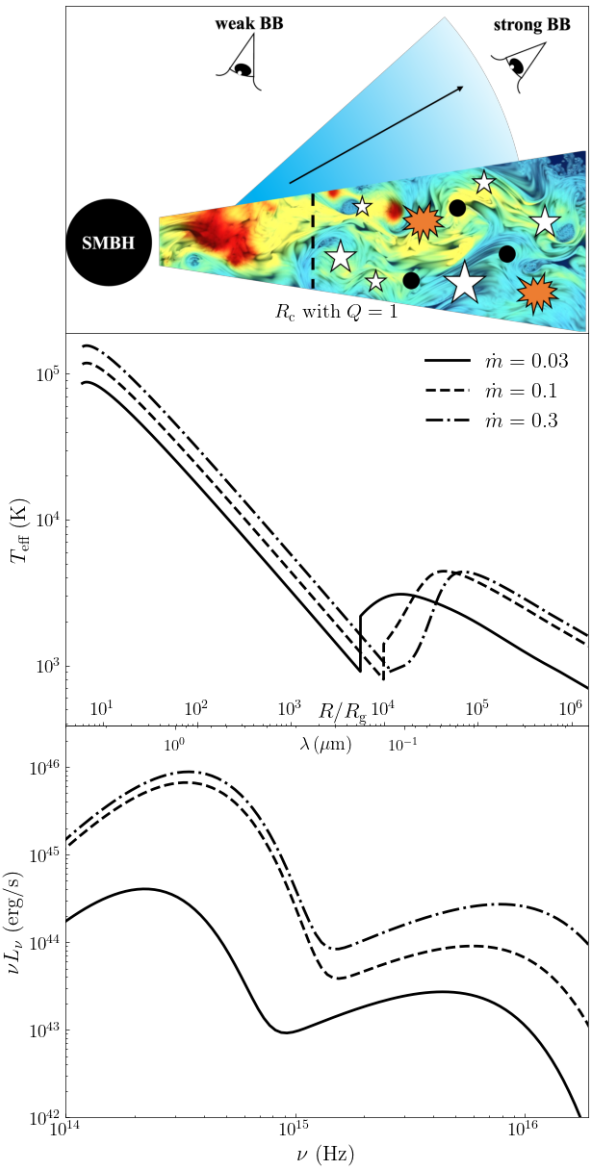

Fig. 3: The top panel shows a cartoon for the inner standard disk and the outer gravitationally unstable disk with disk winds. The strength of Balmer break (BB) depends on whether the line of sight traverses dense gas in the disk wind or not. The distribution of the disk temperature and the corresponding SED are shown in the middle and bottom panels respectively for $M_{\rm BH} = 10^{7.5} M_\odot$ and dimensionless accretion rate of $\dot{m} = \dot{M}/\dot{M}_{\rm Edd} = 0.03, 0.1, 0.3$. This model predicts V-shaped SEDs, where the two components come from the inner standard thin disk and outer marginally unstable disk, respectively.

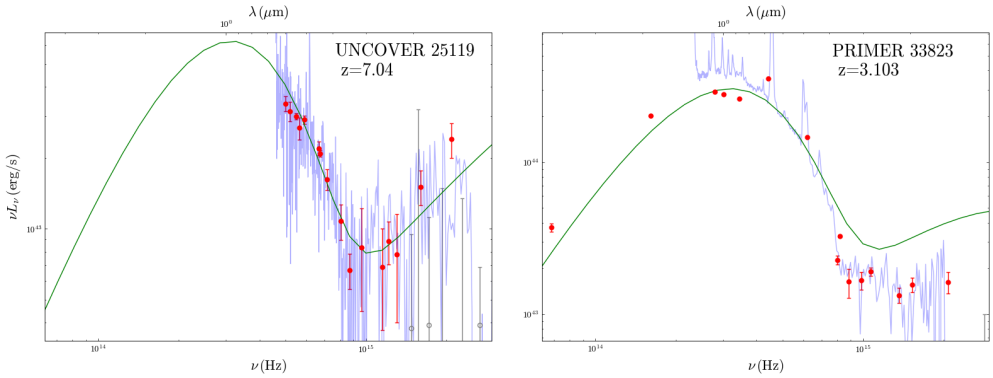

Fig. 4: Examples for the MCMC fittings for the photometric data of the above two LRDs (UNCOVER 25119 and PRIMER 33823) with the composite spectrum from an inner standard disk and an outer gravitationally unstable accretion disk, where the spectroscopic data is also included for comparison and the data points with signal-to-noise ratio (SNR) < 1 are neglected (gray circles). The best fitting parameters are $\dot{M} = 0.22^{+0.03}_{-0.01}\dot{M}_{\rm Edd}$, $R_{\rm out} = 2.62^{+0.07}_{-0.03}R_{\rm c}$ for UNCOVER 25119 and $\dot{M} = 0.01^{+0.01}_{-0.01}\dot{M}_{\rm Edd}$, $R_{\rm out} = 2.41^{+0.01}_{-0.01}R_{\rm c}$ for PRIMER 33823 respectively. The UV emission from the model is about two times higher than the observations in PRIMER 33823, which is possibly caused by the absorption.

results for two LRDs of PRIMER 33823 and UNCOVER 25119, while the fitting for the other 27 sources is presented in Methods 2.4. The V-shaped SED of UNCOVER 25119 can be well fitted using this model with the parameters $\dot{M} = 0.22^{+0.03}_{-0.01}\dot{M}_{\rm Edd}$ and $R_{\rm out} = 2.62^{+0.07}_{-0.03}R_{\rm c}$, with an estimated SMBH mass of $10^{6.89}M_{\odot}$ derived from its broad emission lines, where $\dot{M}_{\rm Edd}$ is the Eddington accretion rate and $R_{\rm c}$ is the critical radius corresponding to $Q = 1$. For PRIMER 33823, the near infrared to optical bump in SED is quite evident because it has the MIRI photometric data (4.9 to 27.9 μm) and is located at a low redshift of $z = 3.1$. The fitting parameters are $\dot{M} = 0.01^{+0.01}_{-0.01}\dot{M}_{\rm Edd}$ and $R_{\rm out} = 2.41^{+0.01}_{-0.01}R_{\rm c}$ when adopting $M = 10^{8.2}M_{\odot}$. The optical-UV emission may be absorbed to some extent, as suggested by the strong Balmer break (BB $\sim$ 2.5, calculated from the median flux ratio between the [4000, 4100] Å and [3620, 3720] Å ranges in the rest-frame following [23]). Similarly, we find that this model can well reproduce the V-shaped SEDs for the other 27 LRDs, with the SMBH masses derived from their broad lines (see Methods 2.4).

The similar break frequencies observed in the V-shaped SEDs of LRDs suggest a common physical mechanism underlying their unique SEDs. Setton et al. [40] proposed that LRDs exhibiting strong changes in spectral slope are highly unlikely to be explained by a two-component AGN model, which accounts for the break through a combination of scattered and attenuated components. In the self-regulated marginally unstable accretion disk model, the V-shaped SEDs arise from a composite spectrum contributed by the inner standard disk and the outer gravitationally unstable disk. Based on typical parameter distributions (e.g., $M_{\rm BH} \sim 10^{6.5-8.5}M_{\odot}$,

$\dot{M} = 0.01 - 0.5\dot{M}_{\rm Edd}$ and $R_{\rm out} = 2 - 5R_{\rm c}$) used to model the LRD SEDs, we find that the break frequencies lie within a narrow range (e.g., $\sim 10^{15\pm0.1}$Hz). Consequently, this model provides a natural explanation without the need to fine-tune numerous model parameters. For supermassive black holes with lower masses (e.g., $M_{\rm BH} \lesssim 10^{6.5} M_{\odot}$), the critical radius of the gravitationally unstable disk is larger in sub-Eddington states, resulting in a lower disk temperature ($\lesssim 1000$ K) and less pronounced infrared emission. If the accretion rates approach or exceed the Eddington limit, the radiation from the inner disk becomes stronger, while the radiation from the outer disk changes less due to the increase in $R_{\rm c}$, which also leads to a lower break frequency in the composite spectrum (see Method 2.3). Variability is a fundamental characteristic of AGNs and can serve as an indicator of fluctuations near the horizons of central supermassive black holes. In our model, the infrared-to-optical and optical-UV emissions originate from the outer disk and the inner disk, which suggests that the variability in infrared-to-optical and optical-UV wavebands may not be correlated on short timescales. Some studies have tentatively explored the variability in LRDs, but no significant variability has been reported [14, 41, 42], despite several LRDs displaying potential variability [14]. Time-domain data from JWST on LRDs remain sparse, and multi-epoch observations for more LRDs across different wavebands, particularly in the ultraviolet band, can be used to test this model.

Balmer break at 3645 Å in the rest frame is evident in some LRDs [18, 43, 44]. The V-shaped spectra of LRDs are proposed to be possibly caused by Balmer break, as their frequencies are relatively similar [40]. This absorption may be a significant factor in some LRDs with extreme Balmer breaks (e.g., Balmer break strength > 3, as seen in Cliff [25]), and it may also be the case in some LRDs in our sample (e.g., CEERS 10444, PRIMER 33823, and UNCOVER 9497). The Balmer absorption lines as observed in the spectra of some LRDs appear to support the idea of AGN absorption in dense gas [9, 25, 45, 46]. However, the break frequency of V-shaped spectra in many LRDs clearly deviates from the Balmer limit (e.g., 1433-1045, JADES-13704 as discussed in Setton et al. [40]) or does not display a strong break near the Balmer limit in many LRDs. This suggests that the Balmer break is not the primary physical mechanism for most V-shaped spectra in LRDs. We note that strong extinction from dust is still necessary to reproduce the V-shaped spectrum of LRDs in the absorption scenario (e.g., $A_V \sim 2-3$, [24, 26]). However, the lack of hot and cold dust emission in most luminous LRDs does not support the dust-attenuated scenario [20, 27, 28]. The Balmer absorption feature as found in the broad lines of some LRDs may originate from dense disk winds [9, 47], where the AGN continuum absorbed by these dense winds can lead to the observed Balmer break. If this is the case, the Balmer break and absorption features should be significant at large viewing angles along the motion of the winds (see cartoon in Figure 3), since that anisotropic disk wind is normally along the disk. In our model, the infrared-to-optical spectral bump arises from emission in the outer gravitationally unstable disk, where the intrinsic Balmer break strength is $\lesssim 1.5$ in model SEDs without considering absorption. From observations, about 10-30% of sources have Balmer break with BB$\gtrsim 1.5$ [44], where the inflection wavelength in V-shaped SEDs will be affected in sources with strong Balmer breaks [25].

The LRDs are typically X-ray weak sources, as evidenced by the nondetection of individual LRDs or the stacked sample in Chandra X-ray data [12, 13]. We estimate the X-ray emission for these LRDs based on the empirical correlation between optical and hard X-ray emissions (characterized by optical to X-ray spectral index $\alpha_{\rm OX}$ and the X-ray spectral index Γ), where the optical emission is derived from our disk modeling of the optical to UV data. Our findings indicate that the X-ray intensity of most LRDs is below the detection limit of *Chandra* (see Method 2.5 for more details). We also estimate the line luminosities using the ionization spectrum from our disk model, based on photoionization calculations performed with CLOUDY simulations [48], where the locally optimally emitting clouds are considered. Excluding five sources with unreasonably large values of covering factor CF > 1, we find that the average CF is approximately 0.3, which is roughly consistent with the typical value in normal AGNs [49]. The unreasonable covering factors in these five LRDs may be attributed to absorption of the continuum or deviations of their spectra from the standard disk model, where those sources all have $\dot{M}/\dot{M}_{\rm Edd} < 5\%$. It should be noted that most LRDs are sub-Eddington sources and their intrinsic luminosities are not so high, which is the main difference for the dust-attenuated models. The total energy output based on multi-wavelength observations for these LRDs can provide a key discriminant between our model and alternative explanations.

The LRDs are common at high redshifts based on JWST observations. The evolution of the LRDs is still a puzzle, and it is unclear why no strong infrared-to-optical emission in other AGNs. The hot dust emission ($\sim 500 - 2000\,{\rm K}$) from the torus is notably absent in LRDs [27], and this deficit may be attributed to low metallicities (e.g., [50, 51]). Gravitational instability in the outer AGN disk provides a pathway for star formation. The embedded stars in AGN disks will accrete quickly in a dense environment and lead to fast metal enrichment after supernova explosion[35]. The increase of metallicity with the evolution of AGNs will lead to more dust in the nuclear region of galaxies. The higher dust opacity will lead to a more inflated disk in the outer region, since the dust opacity sensitively depends on the metallicity [52]. If the optically-thick dust and gas sandwich the outer SG disk, the infrared-to-optical emission from the outer SG disk will be absorbed and re-radiated at longer wavelengths, where the inner radius of the torus is comparable to the size of the SG disk as suggested by near-infrared reverberation mapping (e.g., [53]). This may be the physical reason why the LRDs only appear in high-redshift dwarf galaxies, and the infrared-to-optical emission is suppressed in local AGNs and high redshift QSOs with higher metallicities [35, 54–57]. We note that seven local dwarf galaxies exhibiting V-shaped SEDs have been reported, which show sub-Eddington rates and are potentially local analogs to LRDs [58]. Further searches for possible low-redshift counterparts could provide additional insight into the evolution of LRDs.

2 Methods

2.1 Photometric and Spectroscopic data for LRDs

Kocevski et al. [3] presented a sample of 341 LRDs including the CEERS [59], PRIMER [60], JADES [61], UNCOVER [62], and NGDEEP [63] surveys, where the continuum

slope ($\beta, f_\nu \propto \nu^\beta$) for $\beta_{\rm opt} > 0$ and $\beta_{\rm UV} < -0.37$ were adopted as selection criteria. In this work, we focus on a total of 29 spectra of confirmed LRDs that exhibit broad emission lines. Among them, 26 sources are selected from [3]. We exclude PRIMER-UDS 119639 due to the non-detection at shorter wavelengths, where the V-break spectra are not evident. Furthermore, we also include three additional LRDs: J0647-1045 as reported in [17]; COS 756434 as reported in [64]; and JAEDS 954 as reported in [65] by adopting the selection criteria of $m_{277} - m_{444} > 1.0$. It should be noted that our sample is not complete, where the LRDs with weak UV emission or non-power-law emission may be neglected using the above selection criteria(e.g., MSAID 45954 in [6]).

For sources in UNCOVER survey, we adopt the photometric catalog data from UNCOVER and MegaScience Data Release 3 (DR3) and the NIRSpec MSA spectra data from Data Release 4 [DR4, e.g., 62, 66–68]. The DR3 photometric catalog includes photometry from the combined *MegaScience* and UNCOVER set of mosaics, which incorporate the NIRCam filters (F070W, F090W, F115W, F140M, F150W, F162M, F182M, F200W, F210M, F250M, F277W, F300M, F335M, F356W, F360M, F410M, F430M, F444W, F460M, and F480M), four HST/WFC3 filters (F105W, F125W, F140W, and F160W) and two HST/ACS filters (F606W and F814W). We choose the "SUPER" catalog, which is the recommended photometric catalog with the most suitable aperture sizes. The reduced JWST/NIRSpec PRISM spectroscopy from UNOCOVER and MegaScience DR4 is adopted for these sources.

For sources in JADES survey, we adopt Kron photometry from the photometry catalog data from JADES Data Release 2 and the NIRSpec MSA spectra data from the JADES Data Release 3 [61, 69–72]. The photometric data contains JWST/NIRCAM filters (F090W, F115W, F150W, F182M, F200W, F210M, F277W, F335M, F356W, F410W, F444W for the GOODS-N field and additional F430M, F460M, F480M for the GOODS-S field) and the HST filters (ACS/UV, Optical F435W, F606W, F775W, F814W, F850LP and WFC3/IR F105W, F125W, F140W, F160W). JADES Data Release 3 provides spectroscopy data with three medium gratings (G140M/F100LP, G235M/F170LP, and G395M/F290LP) and the PRISM.

For the sources from CEERS, PRIMER, and MACS0647 surveys, we adopt DJA/-grizli photometric catalogs from the DAWN JWST Archive [DJA, 73, 74]. We adopt the data reduced with an aperture of $0.36''$ in the catalog. CEERS data include JWST/NIRCAM filters (F115W, F150W, F182M, F200W, F210M, F277W, F356W, F410M, F435W, F444W) and HST/WFC3 filters (F105W, F125W, F140W, F160W and HST/ACS filters F606W, F814W). PRIMER survey includes JWST/NIRCAM filters (F090W, F115W, F150W, F200W, F277W, F356W, F410W, F435W, F444W) HST/WFC3 filters (F125W, F140W, F160W) and HST/ACS filters (F606W, F814W). MACS0647 has JWST/NIRCAM filters of F115W, F150W, F200W, F277W, F356W, and F444W. For the source PRIMER 33823, we also include the JWST/MIRI filter of F770W and F1800W. For the LRD of COS 756434, we adopt the photometric data given by [64]. The PRISM spectrum data of PRIMER, MACS0647, and COSMOS are from DJA/msaexp [75, 76] and the PRISM spectra data of CEERS are from CEERS Data Release 0.7 [77, 78]. For UNCOVER 4535, we find that the spectrum needs to be

scaled by a factor of 2 to match the photometric data, which is similar to the source CEERS 1670, as reported in [8] due to the slit loss.

In total, our sample includes 29 LRDs with photometric data and 23 sources with PRISM spectra, where CEERS 69459, PRIMER 116251, and 32438 lost the PRISM observations, and 3 sources in UNCOVER show no valid spectra in DR4.

2.2 The broken power-law fitting for the V-shaped SEDs of LRDs

We present the SEDs of our selected LRDs based on the photometric data shown in Figure 5, where the V-shaped spectral features are evident in most of the sources. We initially fit the V-shaped SED in the rest frame with a simple broken-power-law model, where $\log \nu L_\nu = k_1 \cdot (\log \nu - \log \nu_{\rm b}) + \log \nu L_{\nu {\rm b}}$ and $\log \nu L_\nu = k_2 \cdot (\log \nu - \log \nu_{\rm b}) + \log \nu L_{\nu {\rm b}}$ are adopted for the frequencies lower and higher than the break frequency, $\nu_{\rm b}$, respectively, by using **curve_fit** [79]. The fitting results are shown as solid lines in Figure 5, where the photometric data with frequency higher than the Lyman limit (open circles) or the data with Signal-to-Noise Ratio (SNR) less than 1 (open triangles) are neglected in our fittings in Figures 5. Additionally, we mask data points that are significantly influenced by prominent emission lines—specifically, those exceeding 1.5 times the adjacent continuum or 0.1 times the amplitude of the emission lines (indicated by red squares in Figure 5). This process particularly focuses on the Hα, Hβ, and [OIII] features. The fitting parameters are presented in Table 1. For most LRDs, the fitting yields reasonable results, and the break frequencies of the V-shaped SEDs range from $10^{14.8}$ to $10^{15.1}$ Hz.

2.3 Model of the inner standard disk and the outer gravitationally unstable disk

The spectral energy distributions in this work are derived from the self-gravitating disk model as proposed by [36]. The basic equations of this model are described as follows,

$$\sigma T_{\rm eff}^4 = \frac{3}{8\pi} \dot{M} \Omega_{\rm K}^2 \left[1 - (\frac{R_{\rm in}}{R})^{1/2} \right] \tag{1}$$

$$T_{\rm c}^4 = \left(\frac{3}{8}\tau + \frac{1}{2} + \frac{1}{4\tau} \right) T_{\rm eff}^4, \tag{2}$$

$$\tau = \frac{\kappa \Sigma}{2}, \tag{3}$$

$$c_s^2 \Sigma = \frac{\dot{M} \left[1 - (R_{\rm in}/R)^{1/2} \right] \Omega_{\rm K}}{3\pi\alpha}, \tag{4}$$

$$p_{\rm rad} = \frac{\tau \sigma}{2c} T_{\rm eff}^4, \tag{5}$$

$$p_{\rm gas} = \frac{\rho k T_{\rm c}}{m}, \tag{6}$$

$$\Sigma = 2\rho h, \tag{7}$$

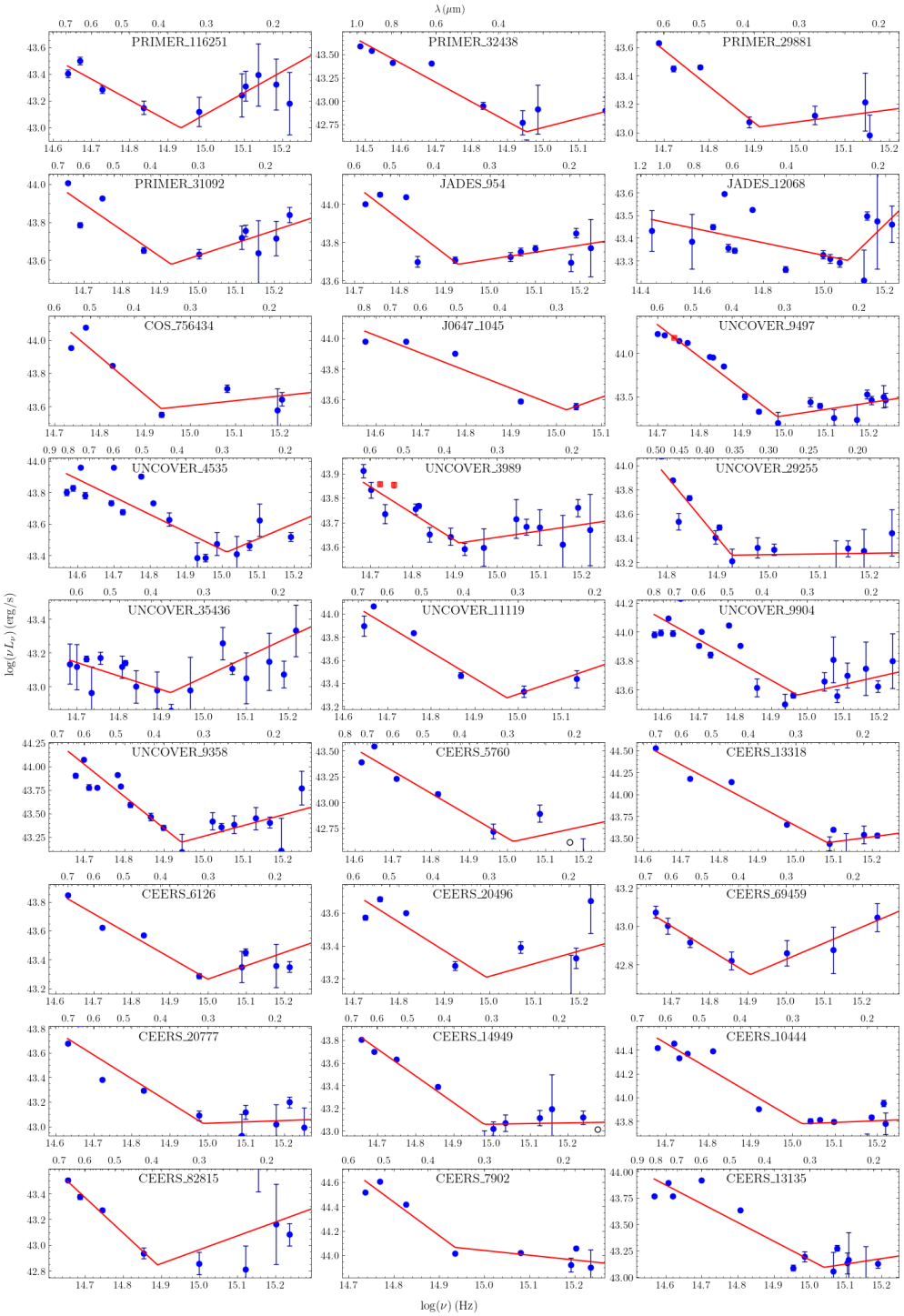

Fig. 5: The photometric SED of LRDs where the data with SNR<1 is shown with black open circles. The V-shaped SED is fitted with a simple broken-power-law function (red solid line), where the red circles that are affected by emission lines are not included in the fitting. The long-wavelength MIRI data of CEERS 14949 and PRIMER 33823 are also neglected in the fitting, where these points evidently deviate from the linear relation (see the model fitting in Figure 7).

$$h = \frac{c_s}{\Omega_{\rm K}}, \tag{8}$$

$$c_s^2 = \frac{p_{\rm gas} + p_{\rm rad}}{\rho}, \tag{9}$$

$$\kappa = \kappa(\rho, T), \tag{10}$$

where $\Omega_{\rm K} = \sqrt{GM_{\rm BH}/R^3}$ is Keplerian angular velocity, $R_{\rm in}$ is inner boundary of accretion disk, and $m = 0.62\, m_{\rm H}$ is the mean molecular mass. Given the black hole mass M, accretion rate $\dot{M_{\rm BH}}$, and viscosity parameter α, these 10 equations can be solved, deriving 10 unknowns: effective temperature $T_{\rm eff}$, midplane temperature $T_{\rm c}$, optical depth τ, surface density Σ, sound speed $c_{\rm s}$, radiation pressure $p_{\rm rad}$, gas pressure $p_{\rm gas}$, gas density ρ, disk half thickness h, and opacity κ at any radius R.

In the outer parts of the disk, once Toomre parameter less than unity (i.e., $Q = c_{\rm s}\Omega_{\rm K}/\pi G\Sigma = \Omega_{\rm K}^2/2\pi G\rho < 1$), the accretion disk is gravitationally unstable and prone to fragment into clumps or even stars [e.g., 33, 80], which may account for the supersolar metallicity of broad line regions [e.g., 32–35]. Sirko & Goodman [36] suggested that the outer disk could evolve toward a marginally stable state with $Q \sim 1$. Chen et al. [38] explored this issue and found that gravitationally unstable ($Q \sim 1$) outer regions of AGN disks are possible based on 3D radiation hydrodynamic local shearing-box simulations. If this is the case, equation 1 is no longer valid, the density of the outer disk is given by $\rho = \Omega_{\rm K}^2/2\pi G$, and $T_{\rm eff}$ should be derived from equation 2.

$R_{\rm in} = 6\, R_{\rm g}$ and $\alpha = 0.1$ are adopted as typical values throughout this work. For the dependency of opacity on density and temperature (equation 10), we use the opacity tables performed by [81] for high temperature regimes ($> 10^{3.75}$ K). In the marginally stable region, the temperature of the disk is relatively low, and the opacity is dominated by dust grains. To account for this, we adopted the opacity tables for low temperature regimes ($< 10^{3.75}$ K) provided by [82], which takes into account the equation of state of the dust fully coupled to the gas.

With the above structure and temperature distribution of the accretion disk, the emitted spectrum is given by

$$L_\nu = \pi \int_{R_{\rm in}}^{R_{\rm out}} \frac{2h\nu^3}{c^2} \frac{2\pi r}{\exp[h\nu/kT_{\rm eff}(R)] - 1} dR, \tag{11}$$

The composite spectra and the disk temperature distribution from this accretion model, with $M_{\rm BH} = 10^{6-9} M_\odot$ and $\dot{M} = 0.01 - 1 \dot{M}_{\rm Edd}$ are shown in Figure 6, where $R_{\rm out} = 10 R_{\rm c}$ is adopted. For $\dot{M} = 0.01 \dot{M}_{\rm Edd}$, the near infrared bump in the SED is less evident for $M_{\rm BH} \lesssim 10^7 M_\odot$ (left panel) due to the lower disk temperature in outer marginally unstable disk (right panel). With increase of accretion rate, the critical SMBH mass for evident infrared bump becomes slightly lower (e.g., $M_{\rm BH} \lesssim 10^6 M_\odot$ for $\dot{M} = 0.3 \dot{M}_{\rm Edd}$). For $\dot{M} \sim \dot{M}_{\rm Edd}$, the break frequencies also become slightly lower, as the optical/UV emissions become much stronger, while the near-infrared to optical emissions remain roughly unchanged due to the increase in $R_{\rm c}$ with growth of the accretion rate. Figure 6 shows that this model can naturally reproduce the V-shaped SEDs with break frequency $\sim 10^{15}$Hz except for some parameter space. This model predicts a black-body structure SED from near infrared to optical waveband, which is mainly contributed by the outer gravitationally unstable disk. The comparison of

more LRDs with mid-infrared data can test this model and distinguish it from other models.

2.4 The fitting of the V-shaped spectrum by the outer gravitationally unstable disk for all LRDs

We present the modeling for all sources now. In this modeling, we consider only two parameters: the accretion rate $\dot{M}$ and the outer radius of the accretion disk $R_{\rm out}$. We adopt the SMBH mass estimated from the broad lines and use a typical value of $\alpha = 0.1$, noting that the spectrum is influenced by the BH mass but is not sensitive to the viscosity parameter. The other two parameters, $\dot{M}$ and $R_{\rm out}$, are treated as free variables that can be constrained through the SED modeling. It is important to note that some photometric data may be significantly affected by the emission lines. Therefore, we also include spectroscopic data to compare with the photometric SEDs, while minimizing the influence of photometric data near prominent emission or absorption lines. The modeling results for all LRDs are shown in Figure 7, where the fitting parameters are presented in Table 1. The posterior distributions of the model parameters for two sources are shown as an example in the Figure 8. We find that the model can well reproduce the observed V-shaped SEDs of most LRDs. The absence of an evident bump in some sources may primarily result from the limited range of observed wavelengths. Several sources exhibit evidence of a curve-like structure in the left part of the spectrum (e.g., CEERS 14949, UNCOVER 9497, UNCOVER 25119; see Figures 5 and 7), which are consistent with the model predictions for PRIMER 33823. The predicted break frequencies in the SEDs align closely with the observed values without the need for extensive fine-tuning of the model parameters. The strength of the infrared bump in LRDs is influenced by parameters of both $\dot{M}$ and $R_{\rm out}$, where $\dot{M}$ can roughly be estimated from the optical/UV observations. Thus, the strength of the infrared bump is mainly governed by the outer radius of the self-regulated marginally unstable disk. We find that $R_{\rm out}/R_{\rm c}$ ranges from 2 to 7 and the dimensionless accretion rates, $\dot{m} = \dot{M}/\dot{M}_{\rm Edd}$, range from 0.004 to 5 in our fitting results, where $\dot{M}_{\rm Edd}$ is Eddington accretion rate. In the SED modeling, we neglect photometric data with SNR < 1 (open gray circle) or affected by emission lines (open red circle) in Figure 7.

2.5 Estimation of the X-ray strength in LRDs

The weak or non-detection of LRDs in X-ray wavebands suggests that their X-ray emission may be intrinsically weak or these LRDs are Compton-thick(e.g., [12, 13]). We estimate the strength of X-ray emission for these LRDs based on the disk emission as constrained from the modeling and the typical AGN SEDs from optical to X-ray wavebands, where the empirical correlation $\alpha_{\rm ox} = -0.14 \times \log L(2500\,\text{Å})$ as constrained from type I AGNs[e.g., 83] and typical unabsorbed X-ray power-law index of $\Gamma \sim 1.7$ are adopted. We find that the predicted observation $2-10$ keV X-ray flux range from $F_{2-10\ \rm keV} \sim 10^{-17} - 10^{-16}$ erg s^{-1} cm^{-2} (see Table 1), which suggests that the X-ray emission of LRDs is intrinsically weak and nearly all LRDs in our sample are below the typical *Chandra* detection limit(e.g., [84]).

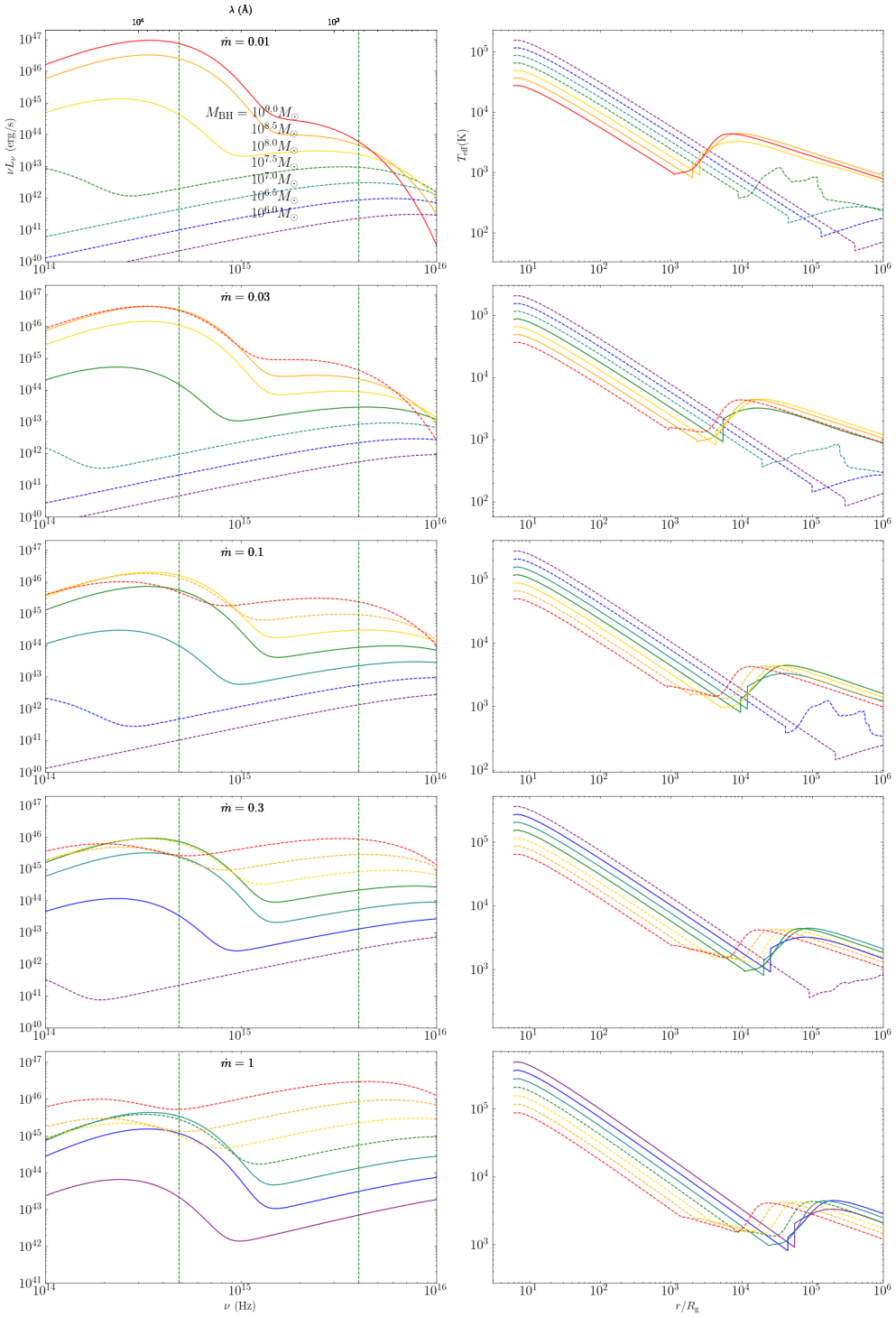

Fig. 6: The SEDs and disk temperature of the adopted model with an inner standard disk and an outer self-regulated disk. The left panels present the disk SEDs with different accretion rates with $R_{\rm out} = 10R_{\rm c}$, while the right panels show the distribution of the effective disk temperature for the adopted parameters in the other three panels. Green lines show the corresponding wavelength coverage of NIRCam at $z = 7$.

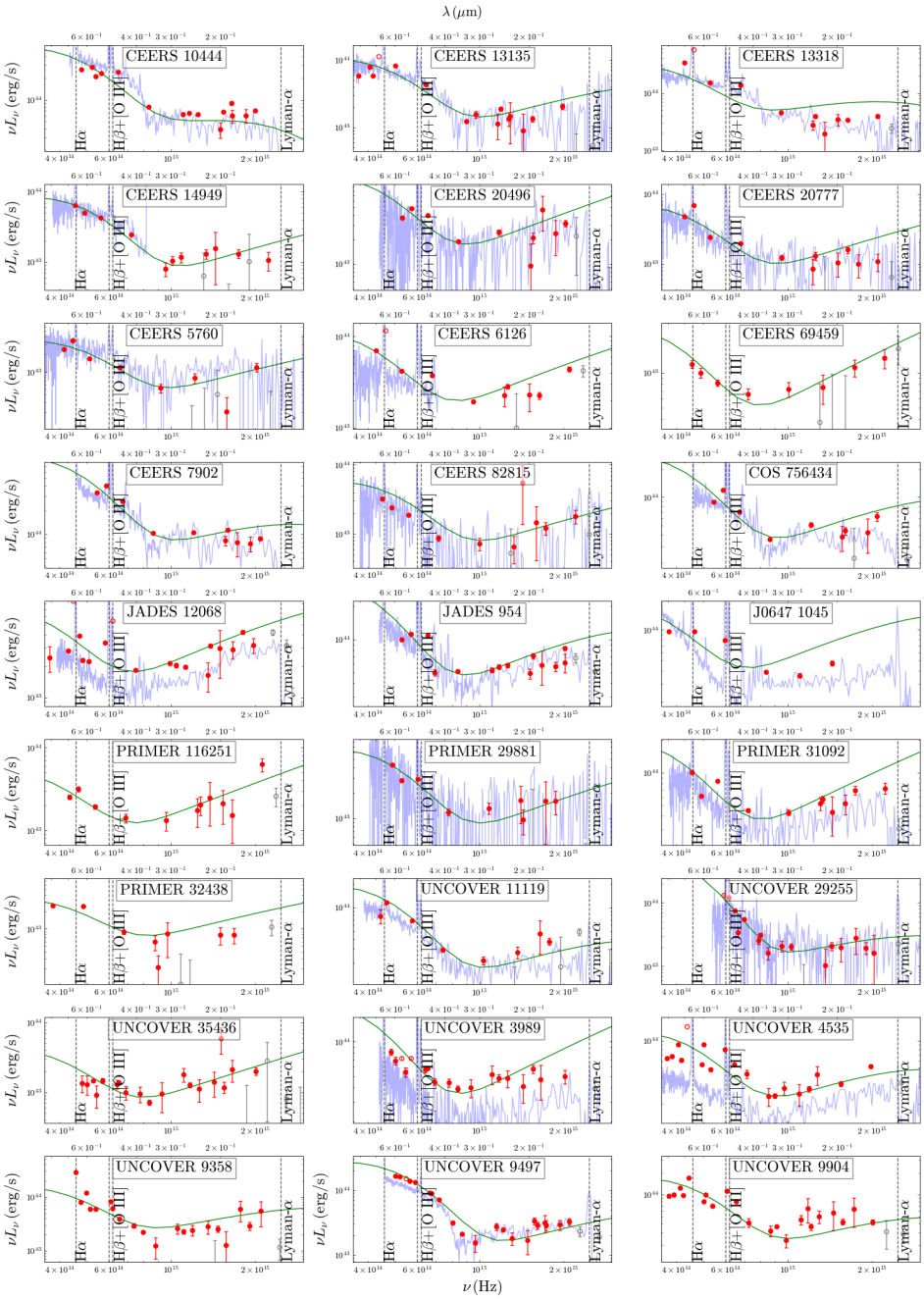

Fig. 7: The model fitting for the V-shaped SEDs of LRDs (solid line) based on the MCMC method, where the photometric and spectrometric data are presented for comparison. Data points affected by the line emission are shown as red open circles. The data have an SNR lower than 1 are shown with black open circles.

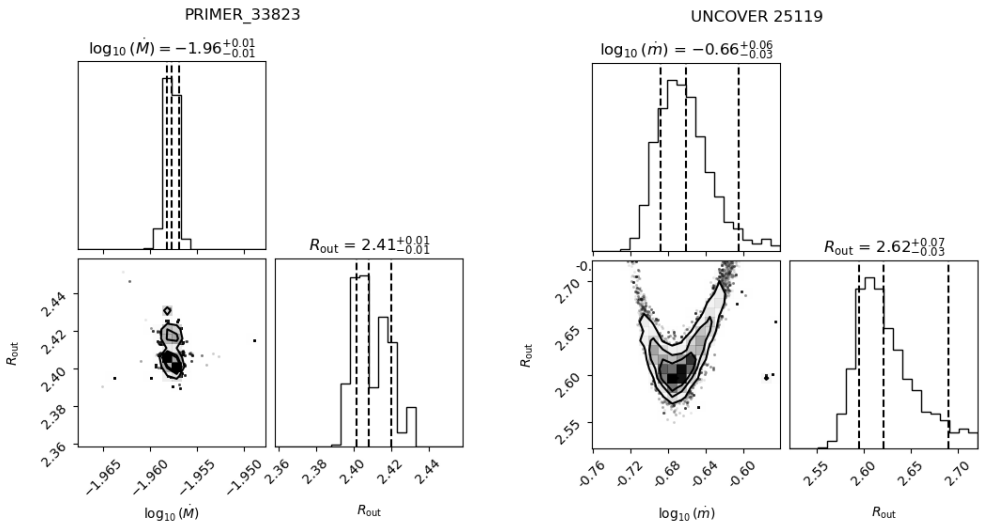

(a) (b)

Fig. 8: The posterior distributions of the model parameters including the dimensionless accretion rate and the outer radius of accretion disk for two sources as an example.

2.6 Estimation of the broad-line strength in LRDs

We also tentatively estimate the strength of the broad Balmer lines based on the photoionization model that is widely adopted to investigate the optical emission lines in AGNs, where CLOUDY code version C23.01 is adopted with pyCloudy [48, 85]. We simply describe the model here(see [86] for more details). The locally optimally emitting cloud model was implemented to calculate emission line intensities, which assumes that substantial emission for any given spectral line originates exclusively within a narrow photoinization parameter range (e.g., [87, 88]). The line flux from individual cloud surfaces is characterized by $F(r, n)$, where r represents the distance from the central source and n denotes the plasma number density. The total broad-line luminosities can be estimated from $L_{\rm line} \propto \iint r^2 F(r, n) f(r) g(n)\, {\rm d}n{\rm d}r$, where $f(r)$ and $g(n)$ describe the radial distribution and density distribution functions of clouds respectively. In our simulations, BLR clouds are modeled with solar metallicity and a hydrogen column density of $N_{\rm H} = 10^{23}{\rm cm}^{-2}$. The number density spans $10^8 - 10^{14}{\rm cm}^{-3}$ with logarithmic grid steps of 0.1 dex for density and 0.2 dex for radial distance are adopted.

The SEDs from accretion disk are set as incident AGN continuum(see Method 2.3). To reproduce the observed broad Hα line luminosities, we find that the covering factors (CF) range from 0.03 to 14.45. Five sources with CF$>$ 1 have very low Eddington ratios (e.g., less than several percent), where the intrinsic SEDs from standard disks may not be a good approximation. Excluding these five sources, we find the average CF is 0.3, which is roughly consistent with the typical value in type I AGNs [49].

Acknowledgements. CZ and QW are supported by National Natural Science Foundation of China (grants 12233007 and CMS-CSST-2025-A07) and the National Key Research and Development Program of China (No. 2023YFC2206702). LCH was supported by the National Science Foundation of China (11991052, 12233001), the National Key R&D Program of China (2022YFF0503401), and the China Manned Space Project (CMS-CSST-2021-A04, CMS-CSST-2021-A06). HZ acknowledges the National Science Foundation of China grant (No. 12303007)

Declarations

- Data availability The data underlying this article will be shared on the request to the corresponding author.
- Code availability The codes are available on the request to the corresponding author.

References

[1] Gardner, J. P. et al. The James Webb Space Telescope Mission. Publ. Astron. Soc. Pac. **135**, 068001 (2023).

[2] Onoue, M. et al. A Candidate for the Least-massive Black Hole in the First 1.1 Billion Years of the Universe. Astrophys. J. Lett. **942**, L17 (2023).

[3] Kocevski, D. D. et al. The Rise of Faint, Red AGN at $z > 4$: A Sample of Little Red Dots in the JWST Extragalactic Legacy Fields. arXiv e-prints arXiv:2404.03576 (2024).

[4] Chen, C.-H., Ho, L. C., Li, R. & Zhuang, M.-Y. The Host Galaxy (If Any) of the Little Red Dots. arXiv e-prints arXiv:2411.04446 (2024).

[5] Labbé, I. et al. A population of red candidate massive galaxies 600 Myr after the Big Bang. Nature **616**, 266–269 (2023).

[6] Greene, J. E. et al. UNCOVER Spectroscopy Confirms the Surprising Ubiquity of Active Galactic Nuclei in Red Sources at z ¿ 5. Astrophys. J. **964**, 39 (2024).

[7] Matthee, J. et al. Little Red Dots: An Abundant Population of Faint Active Galactic Nuclei at z $\sim$ 5 Revealed by the EIGER and FRESCO JWST Surveys. Astrophys. J. **963**, 129 (2024).

[8] Kocevski, D. D. et al. Hidden Little Monsters: Spectroscopic Identification of Low-mass, Broad-line AGNs at z ¿ 5 with CEERS. Astrophys. J. Lett. **954**, L4 (2023).

[9] Rusakov, V. et al. JWST's little red dots: an emerging population of young, low-mass AGN cocooned in dense ionized gas. arXiv e-prints arXiv:2503.16595 (2025).

[10] Wang, Z. et al. The Role of Population III Star Tidal Disruption Events in Black Hole Growth at the Cosmic Dawn. arXiv e-prints arXiv:2504.18144 (2025).

[11] Taylor, A. J. et al. Broad-Line AGN at 3.5¡z¡6: The Black Hole Mass Function and a Connection with Little Red Dots. arXiv e-prints arXiv:2409.06772 (2024).

[12] Yue, M. et al. Stacking X-ray Observations of "Little Red Dots": Implications for their AGN Properties. arXiv e-prints arXiv:2404.13290 (2024).

[13] Ananna, T. T., Bogdán, Á., Kovács, O. E., Natarajan, P. & Hickox, R. C. X-ray View of Little Red Dots: Do They Host Supermassive Black Holes? arXiv e-prints arXiv:2404.19010 (2024).

[14] Zhang, Z., Jiang, L., Liu, W. & Ho, L. C. Analysis of Multi-epoch JWST Images of $\sim$ 300 Little Red Dots: Tentative Detection of Variability in a Minority of Sources. arXiv e-prints arXiv:2411.02729 (2024).

[15] Fan, X., Bañados, E. & Simcoe, R. A. Quasars and the Intergalactic Medium at Cosmic Dawn. Annu. Rev. Astron. Astrophys. **61**, 373–426 (2023).

[16] Ye, G., Zhang, H. & Wu, Q. Machine Learning–based Search of High-redshift Quasars. Astrophys. J. Suppl. Ser. **275**, 19 (2024).

[17] Killi, M. et al. Deciphering the JWST spectrum of a 'little red dot' at $z \sim 4.53$: An obscured AGN and its star-forming host. arXiv e-prints arXiv:2312.03065 (2023).

[18] Wang, B. et al. RUBIES: JWST/NIRSpec Confirmation of an Infrared-luminous, Broad-line Little Red Dot with an Ionized Outflow. arXiv e-prints arXiv:2403.02304 (2024).

[19] Pérez-González, P. G. et al. What Is the Nature of Little Red Dots and what Is Not, MIRI SMILES Edition. Astrophys. J. **968**, 4 (2024).

[20] Williams, C. C. et al. The Galaxies Missed by Hubble and ALMA: The Contribution of Extremely Red Galaxies to the Cosmic Census at 3 ¡ z ¡ 8. Astrophys. J. **968**, 34 (2024).

[21] Ma, Y. et al. UNCOVER: 404 Error – Models Not Found for the Triply Imaged Little Red Dot A2744-QSO1. arXiv e-prints arXiv:2410.06257 (2024).

[22] Baggen, J. F. W. et al. The Small Sizes and High Implied Densities of 'Little Red Dots' with Balmer Breaks Could Explain Their Broad Emission Lines Without an AGN. arXiv e-prints arXiv:2408.07745 (2024).

[23] Wang, B. et al. RUBIES: Evolved Stellar Populations with Extended Formation Histories at z $\sim$ 7–8 in Candidate Massive Galaxies Identified with

JWST/NIRSpec. Astrophys. J. Lett. **969**, L13 (2024).

[24] Inayoshi, K. & Maiolino, R. Extremely Dense Gas around Little Red Dots and High-redshift Active Galactic Nuclei: A Nonstellar Origin of the Balmer Break and Absorption Features. Astrophys. J. Lett. **980**, L27 (2025).

[25] de Graaff, A. et al. A remarkable Ruby: Absorption in dense gas, rather than evolved stars, drives the extreme Balmer break of a Little Red Dot at $z = 3.5$. arXiv e-prints arXiv:2503.16600 (2025).

[26] Ji, X. et al. BlackTHUNDER – A non-stellar Balmer break in a black hole-dominated little red dot at $z = 7.04$. arXiv e-prints arXiv:2501.13082 (2025).

[27] Setton, D. J. et al. A confirmed deficit of hot and cold dust emission in the most luminous Little Red Dots. arXiv e-prints arXiv:2503.02059 (2025).

[28] Xiao, M. et al. No [CII] or dust detection in two Little Red Dots at $z_{\rm spec}$ ¿ 7. arXiv e-prints arXiv:2503.01945 (2025).

[29] Casey, C. M. et al. Dust in Little Red Dots. Astrophys. J. Lett. **975**, L4 (2024).

[30] Shakura, N. I. & Sunyaev, R. A. Black holes in binary systems. Observational appearance. Astron. Astrophys. **24**, 337–355 (1973).

[31] Toomre, A. On the gravitational stability of a disk of stars. Astrophys. J. **139**, 1217–1238 (1964).

[32] Shlosman, I. & Begelman, M. C. Self-gravitating accretion disks in active galactic nuclei. Nature **329**, 810–812 (1987).

[33] Goodman, J. Self-gravity and quasi-stellar object discs. Mon. Not. R. Astron. Soc. **339**, 937–948 (2003).

[34] Wang, J.-M. et al. Star Formation in Self-gravitating Disks in Active Galactic Nuclei. III. Efficient Production of Iron and Infrared Spectral Energy Distributions. Astrophys. J. **954**, 84 (2023).

[35] Fan, X. & Wu, Q. In Situ Star Formation in Accretion Disks and Explanation of Correlation between the Black Hole Mass and Metallicity in Active Galactic Nuclei. Astrophys. J. **944**, 159 (2023).

[36] Sirko, E. & Goodman, J. Spectral energy distributions of marginally self-gravitating quasi-stellar object discs. Mon. Not. R. Astron. Soc. **341**, 501–508 (2003).

[37] Gilbaum, S. & Stone, N. C. Feedback-dominated Accretion Flows. Astrophys. J. **928**, 191 (2022).

[38] Chen, Y.-X., Jiang, Y.-F., Goodman, J. & Ostriker, E. C. 3D Radiation Hydrodynamic Simulations of Gravitational Instability in AGN Accretion Disks: Effects of Radiation Pressure. Astrophys. J. **948**, 120 (2023).

[39] Foreman-Mackey, D., Hogg, D. W., Lang, D. & Goodman, J. emcee: The MCMC Hammer. Publ. Astron. Soc. Pac. **125**, 306 (2013).

[40] Setton, D. J. et al. Little Red Dots at an Inflection Point: Ubiquitous "V-Shaped" Turnover Consistently Occurs at the Balmer Limit. arXiv e-prints arXiv:2411.03424 (2024).

[41] Kokubo, M. & Harikane, Y. Challenging the AGN scenario for JWST/NIRSpec broad Hα emitters/Little Red Dots in light of non-detection of NIRCam photometric variability and X-ray. arXiv e-prints arXiv:2407.04777 (2024).

[42] Tee, W. L., Fan, X., Wang, F. & Yang, J. Lack of Rest-frame Ultraviolet Variability in Little Red Dots Based on HST and JWST Observations. Astrophys. J. Lett. **983**, L26 (2025).

[43] Furtak, L. J. et al. JWST UNCOVER: Extremely Red and Compact Object at z $_{phot} \approx$ 7.6 Triply Imaged by A2744. Astrophys. J. **952**, 142 (2023).

[44] Kuruvanthodi, A. et al. Strong Balmer break objects at z $\sim$ 7–10 uncovered with JWST. Astron. Astrophys. **691**, A310 (2024).

[45] Akins, H. B. et al. Strong Rest-UV Emission Lines in a "Little Red Dot" Active Galactic Nucleus at z = 7: Early Supermassive Black Hole Growth alongside Compact Massive Star Formation? Astrophys. J. Lett. **980**, L29 (2025).

[46] D'Eugenio, F. et al. BlackTHUNDER strikes twice: rest-frame Balmer-line absorption and high Eddington accretion rate in a Little Red Dot at $z = 7.04$. arXiv e-prints arXiv:2503.11752 (2025).

[47] Labbe, I. et al. An unambiguous AGN and a Balmer break in an Ultraluminous Little Red Dot at z=4.47 from Ultradeep UNCOVER and All the Little Things Spectroscopy. arXiv e-prints arXiv:2412.04557 (2024).

[48] Chatzikos, M. et al. The 2023 Release of Cloudy. Rev. Mexicana Astron. Astrofis. **59**, 327–343 (2023).

[49] Ferland, G. J., Done, C., Jin, C., Landt, H. & Ward, M. J. State-of-the-art AGN SEDs for photoionization models: BLR predictions confront the observations. Mon. Not. R. Astron. Soc. **494**, 5917–5922 (2020).

[50] Tripodi, R. et al. HYPERION: Coevolution of supermassive black holes and galaxies at z ¿ 6 and the build-up of massive galaxies. Astron. Astrophys. **689**, A220 (2024).

[51] Nakane, M. et al. Fe Abundances of Early Galaxies at $z = 9 - 12$ Derived with Deep JWST Spectra. arXiv e-prints arXiv:2503.11457 (2025).

[52] Baskin, A. & Laor, A. Dust inflated accretion disc as the origin of the broad line region in active galactic nuclei. Mon. Not. R. Astron. Soc. **474**, 1970–1994 (2018).

[53] Nelson, B. O. A Correlated Optical-Infrared Outburst of Markarian 744: The Strongest Evidence Yet for Thermal Dust Reverberation. Astrophys. J. Lett. **465**, L87 (1996).

[54] Xu, F. et al. The evolution of chemical abundance in quasar broad line region. Mon. Not. R. Astron. Soc. **480**, 345–357 (2018).

[55] Onoue, M. et al. No Redshift Evolution in the Broad-line-region Metallicity up to z = 7.54: Deep Near-infrared Spectroscopy of ULAS J1342+0928. Astrophys. J. **898**, 105 (2020).

[56] Śniegowska, M. et al. High Metal Content of Highly Accreting Quasars. Astrophys. J. **910**, 115 (2021).

[57] Wang, S. et al. Metallicity in Quasar Broad-line Regions at Redshift 6. Astrophys. J. **925**, 121 (2022).

[58] Lin, R. et al. Discovery of Local Analogs to JWST's Little Red Dots. arXiv e-prints arXiv:2412.08396 (2024).

[59] Finkelstein, S. L. et al. A Long Time Ago in a Galaxy Far, Far Away: A Candidate z $\sim$ 12 Galaxy in Early JWST CEERS Imaging. Astrophys. J. Lett. **940**, L55 (2022).

[60] Dunlop, J. S. et al. PRIMER: Public Release IMaging for Extragalactic Research. JWST Proposal. Cycle 1, ID. #1837 (2021).

[61] Eisenstein, D. J. et al. Overview of the JWST Advanced Deep Extragalactic Survey (JADES). arXiv e-prints arXiv:2306.02465 (2023).

[62] Bezanson, R. et al. The JWST UNCOVER Treasury survey: Ultradeep NIRSpec and NIRCam ObserVations before the Epoch of Reionization. arXiv e-prints arXiv:2212.04026 (2022).

[63] Bagley, M. B. et al. The Next Generation Deep Extragalactic Exploratory Public (NGDEEP) Survey. Astrophys. J. Lett. **965**, L6 (2024).

[64] Akins, H. B. et al. COSMOS-Web: The over-abundance and physical nature of "little red dots"–Implications for early galaxy and SMBH assembly. arXiv e-prints arXiv:2406.10341 (2024).

[65] Maiolino, R. et al. JADES. The diverse population of infant Black Holes at 4¡z¡11: merging, tiny, poor, but mighty. arXiv e-prints arXiv:2308.01230 (2023).

[66] Suess, K. A. et al. Medium Bands, Mega Science: a JWST/NIRCam Medium-Band Imaging Survey of Abell 2744. arXiv e-prints arXiv:2404.13132 (2024).

[67] Weaver, J. R. et al. The UNCOVER Survey: A First-look HST + JWST Catalog of 60,000 Galaxies near A2744 and beyond. Astrophys. J. Suppl. Ser. **270**, 7 (2024).

[68] Price, S. H. et al. The UNCOVER Survey: First Release of Ultradeep JWST/NIRSpec PRISM spectra for ~700 galaxies from z~0.3-13 in Abell 2744. arXiv e-prints arXiv:2408.03920 (2024).

[69] Eisenstein, D. J. et al. The JADES Origins Field: A New JWST Deep Field in the JADES Second NIRCam Data Release. arXiv e-prints arXiv:2310.12340 (2023).

[70] Bunker, A. J. et al. JADES NIRSpec Initial Data Release for the Hubble Ultra Deep Field: Redshifts and Line Fluxes of Distant Galaxies from the Deepest JWST Cycle 1 NIRSpec Multi-Object Spectroscopy. arXiv e-prints arXiv:2306.02467 (2023).

[71] Rieke, M. J. et al. JADES Initial Data Release for the Hubble Ultra Deep Field: Revealing the Faint Infrared Sky with Deep JWST NIRCam Imaging. Astrophys. J. Suppl. Ser. **269**, 16 (2023).

[72] D'Eugenio, F. et al. JADES Data Release 3 – NIRSpec/MSA spectroscopy for 4,000 galaxies in the GOODS fields. arXiv e-prints arXiv:2404.06531 (2024).

[73] Brammer, G. grizli (2023). URL https://doi.org/10.5281/zenodo.8370018.

[74] Valentino, F. et al. An Atlas of Color-selected Quiescent Galaxies at z ¿ 3 in Public JWST Fields. Astrophys. J. **947**, 20 (2023).

[75] Heintz, K. E. et al. Strong damped Lyman-α absorption in young star-forming galaxies at redshifts 9 to 11. Science **384**, 890–894 (2024).

[76] Brammer, G. msaexp: Nirspec analyis tools (2023). URL https://doi.org/10.5281/zenodo.8319596.

[77] Bagley, M. B. et al. CEERS Epoch 1 NIRCam Imaging: Reduction Methods and Simulations Enabling Early JWST Science Results. Astrophys. J. Lett. **946**, L12 (2023).

[78] Arrabal Haro, P. et al. Spectroscopic Confirmation of CEERS NIRCam-selected Galaxies at z ≈ 8-10. Astrophys. J. Lett. **951**, L22 (2023).

[79] Vugrin, K. W., Swiler, L. P., Roberts, R. M., Stucky-Mack, N. J. & Sullivan, S. P. Confidence region estimation techniques for nonlinear regression in groundwater flow: Three case studies. Water Resources Research **43**, W03423 (2007).

[80] Paczynski, B. A model of selfgravitating accretion disk. Acta Astron. **28**, 91–109 (1978).

[81] Iglesias, C. A. & Rogers, F. J. Updated Opal Opacities. Astrophys. J. **464**, 943 (1996).

[82] Ferguson, J. W. et al. Low-Temperature Opacities. Astrophys. J. **623**, 585–596 (2005).

[83] Steffen, A. T. et al. The X-Ray-to-Optical Properties of Optically Selected Active Galaxies over Wide Luminosity and Redshift Ranges. Astron. J. **131**, 2826–2842 (2006).

[84] Elvis, M. et al. The Chandra COSMOS Survey. I. Overview and Point Source Catalog. Astrophys. J. Suppl. Ser. **184**, 158–171 (2009).

[85] Morisset, C. pyCloudy: Tools to manage astronomical Cloudy photoionization code. Astrophysics Source Code Library, record ascl:1304.020 (2013).

[86] Wu, J. et al. The Weakness of Soft X-Ray Intensity: Possible Physical Reason for Weak-line Quasars. Astrophys. J. **965**, 84 (2024).

[87] Baldwin, J., Ferland, G., Korista, K. & Verner, D. Locally Optimally Emitting Clouds and the Origin of Quasar Emission Lines. Astrophys. J. Lett. **455**, L119 (1995).

[88] Ferland, G. J. Quantitative Spectroscopy of Photoionized Clouds. Annu. Rev. Astron. Astrophys. **41**, 517–554 (2003).

[89] Harikane, Y. et al. A JWST/NIRSpec First Census of Broad-line AGNs at z = 4-7: Detection of 10 Faint AGNs with M $_{BH}$ 10^6-10^8 M $_\odot$ and Their Host Galaxy Properties. Astrophys. J. **959**, 39 (2023).

Table 1: Columns 1 to 4 represent the Name, position, and redshift for the selected LRDs. Column 5 represents the Balmer-break strength (BBs) derived from following the definition as [23]. The BH mass and Hα line luminosity are presented in Column xxx and xxx, which are adopted from literature, where the references for the BH mass are *a*) [89]; *b*) [8]; *c*) [3]; *d*) [64]; *e*) [65]; *f*) [17]; *g*) [6]. Note that the black hole masses of CEERS 69459 and the sources in the UNCOVER survey were derived from the intrinsic luminosity and line width of $H\alpha$ emission in this work. The break frequency, dimensionless accretion rate, and the outer radius of the self-regulated disk are provided in columns 8-10 based on the fitting of the V-shaped SEDs for the selected LRDs. In column 12, we present the estimated covering factor of the broad emission line region. In column 13, we present the predicted X-ray flux at observation frame $2-10$kev based on our model SED and the empirical correlations between optical and X-ray from the normal AGNs.

Name	RA (deg)	Dec (deg)	z	BBs	$\log M_{\rm BH}$ ($M_\odot$)	$\log L_{\rm H\alpha}$ (erg s^{-1})	Refs	$\log \nu_{\rm b}$ (Hz)	$\log \dot{m}$ ($R_{\rm c}$)	$R_{\rm out}$	CF	$F_{2-10{\rm keV}}$ (erg s^{-1} cm^{-2})
CEERS 69459	214.889667	52.832972	5.666	–	6.66	42.03	*a*	$14.91^{\pm0.03}$	$-0.27^{+0.05}_{-0.08}$	$2.37^{+0.11}_{-0.11}$	0.07	1.67×10^{-17}
CEERS 82815	214.809142	52.868484	5.624	0.46	6.95	42.22	*b*	$14.89^{\pm0.12}$	$-0.74^{+0.08}_{-0.13}$	$2.47^{+0.65}_{-0.17}$	0.18	1.87×10^{-17}
CEERS 5760	214.972445	52.962196	5.079	1.48	6.72	–	*c*	$15.02^{\pm0.16}$	$-0.54^{+0.04}_{-0.04}$	$2.42^{+0.19}_{-0.06}$	0.12	1.82×10^{-17}
CEERS 6126	214.923377	52.925588	5.288	–	7.18	–	*c*	$15.00^{\pm0.05}$	$-0.46^{+1.33}_{-0.02}$	$3.45^{+1.90}_{-0.12}$	0.38	4.29×10^{-17}
CEERS 7902	214.983026	52.956001	6.986	2.40	8.24	–	*c*	$14.94^{\pm0.06}$	$-1.59^{+0.01}_{-0.01}$	$3.42^{+0.06}_{-0.05}$	–	5.22×10^{-17}
CEERS 10444	214.892248	52.87741	6.687	2.88	8.57	–	*c*	$15.02^{\pm0.07}$	$-2.34^{+2.70}_{-0.01}$	$2.33^{+2.15}_{-0.01}$	–	3.99×10^{-17}
CEERS 13135	214.886792	52.855381	4.955	3.90	7.39	–	*c*	$15.04^{\pm0.06}$	$-1.19^{+0.01}_{-0.01}$	$2.42^{+0.01}_{-0.01}$	0.52	3.50×10^{-17}
CEERS 13318	214.795368	52.788847	5.280	2.09	8.34	–	*c*	$15.08^{\pm0.06}$	$-1.97^{+0.01}_{-0.01}$	$2.50^{+0.02}_{-0.01}$	14.45	7.01×10^{-17}
CEERS 14949	214.990977	52.916524	5.684	–	6.95	–	*c*	$14.98^{\pm0.05}$	$-0.72^{+0.11}_{-0.02}$	$2.76^{+0.03}_{-0.02}$	0.34	1.88×10^{-17}
CEERS 20496	215.078259	52.948497	6.786	1.60	6.45	–	*c*	$14.99^{\pm0.15}$	$0.81^{+0.03}_{-0.03}$	$5.60^{+0.21}_{-0.22}$	–	2.27×10^{-17}
CEERS 20777	215.137081	52.988554	5.286	0.84	6.84	–	*c*	$14.99^{\pm0.09}$	$-0.31^{+0.03}_{-0.03}$	$2.95^{+0.02}_{-0.02}$	0.30	2.63×10^{-17}
PRIMER 29881	34.313132	-5.226765	6.170	2.01	6.98	–	*c*	$14.91^{\pm0.06}$	$-0.73^{+0.10}_{-0.05}$	$2.56^{+0.14}_{-0.05}$	0.28	1.64×10^{-17}
PRIMER 31092	34.264581	-5.232544	5.675	0.85	7.10	–	*c*	$14.93^{\pm0.07}$	$0.12^{+0.02}_{-0.02}$	$4.97^{+0.12}_{-0.11}$	0.38	5.72×10^{-17}
PRIMER 32438	34.241809	-5.239401	3.500	–	6.98	–	*c*	$14.95^{\pm0.08}$	$-0.68^{+0.04}_{-0.02}$	$2.28^{+0.05}_{-0.06}$	–	5.63×10^{-17}
PRIMER 33823	34.244190	-5.245834	3.103	2.51	8.16	–	*c*	$15.07^{\pm0.10}$	$-1.96^{+0.01}_{-0.01}$	$2.41^{+0.01}_{-0.01}$	10.00	1.35×10^{-16}
PRIMER 116251	34.260537	-5.209120	5.365	–	6.44	–	*c*	$14.93^{\pm0.08}$	$0.75^{+0.07}_{-0.08}$	$4.68^{+0.36}_{-0.30}$	0.03	3.41×10^{-17}
COS 756434	150.106900	2.360046	6.999	2.05	7.80	42.16	*d*	$14.94^{\pm0.07}$	$-1.28^{+0.02}_{-0.02}$	$2.90^{+0.02}_{-0.02}$	0.38	3.28×10^{-17}
JADES 12068	53.12654	-27.81809	5.919	1.28	7.50	42.01	*e*	$15.08^{\pm0.07}$	$-1.05^{+0.01}_{-0.01}$	$2.39^{+0.04}_{-0.03}$	0.11	2.59×10^{-17}
JADES 954	189.15197	62.25964	6.760	1.36	7.90	43.00	*e*	$14.93^{\pm0.05}$	$-1.29^{+0.01}_{-0.01}$	$3.00^{+0.06}_{-0.05}$	2.63	9.68×10^{-17}
J0647 1045	101.933406	70.198268	4.532	0.76	7.90	42.48	*f*	$15.02^{\pm0.07}$	$-1.22^{+0.01}_{-0.02}$	$2.99^{+0.05}_{-0.06}$	0.49	5.93×10^{-17}
UNCOVER 3989	3.533994	-30.353307	6.770	0.68	7.14	42.41	*g*	$14.91^{\pm0.04}$	$-0.04^{+0.02}_{-0.03}$	$4.55^{+0.08}_{-0.07}$	0.24	3.70×10^{-17}
UNCOVER 4535	3.530005	-30.358017	4.962	1.43	7.88	42.58	*g*	$15.01^{\pm0.05}$	$-1.68^{+0.01}_{-0.01}$	$2.10^{+0.01}_{-0.01}$	0.83	5.03×10^{-17}
UNCOVER 9358	3.620612	-30.399949	6.354	1.87	7.82	42.92	*g*	$14.94^{\pm0.04}$	$-1.49^{+0.02}_{-0.01}$	$2.47^{+0.18}_{-0.06}$	1.91	3.32×10^{-17}
UNCOVER 9497	3.579833	-30.401568	7.029	3.47	7.30	–	*g*	$14.98^{\pm0.02}$	$-1.05^{+0.04}_{-0.05}$	$3.37^{+0.14}_{-0.03}$	–	1.78×10^{-17}
UNCOVER 9904	3.550837	-30.406602	5.054	1.79	7.83	42.18	*g*	$14.97^{\pm0.06}$	$-1.62^{+0.01}_{-0.01}$	$2.31^{+0.01}_{-0.01}$	0.40	4.75×10^{-17}
UNCOVER 11119	3.619197	-30.423267	5.835	1.21	7.65	42.73	*g*	$14.98^{\pm0.06}$	$-1.53^{+0.25}_{-0.02}$	$3.11^{+0.26}_{-0.37}$	1.91	2.79×10^{-17}
UNCOVER 25119	3.569590	-30.373221	7.038	2.59	6.89	42.12	*g*	$15.02^{\pm0.02}$	$-0.66^{+0.06}_{-0.03}$	$2.62^{+0.07}_{-0.03}$	0.15	1.14×10^{-17}
UNCOVER 29255	3.640414	-30.386432	8.504	2.02	7.81	–	*g*	$14.93^{\pm0.03}$	$-1.81^{+0.01}_{-0.01}$	$7.47^{+1.42}_{-1.38}$	–	1.27×10^{-17}
UNCOVER 35436	3.592416	-30.432824	6.741	1.31	6.40	42.77	*g*	$14.92^{\pm0.09}$	$0.54^{+0.03}_{-0.03}$	$3.94^{+0.03}_{-0.03}$	0.30	1.59×10^{-17}